

A High Load Density Miniature Force Sensor for Probing With Robot Feet

Jianfeng Zhou , Jiaji Su , Kaiwen Zuo , Mingyu Pan , Zonghe Chua , and Kathryn A. Daltorio 

Abstract—Force sensing on the end effector is crucial for mobile, legged robots to adapt to varying terrain and manipulate objects in complex environments. Since efficient legs have to be light and load bearing, force sensors need to have increased *load density* while still providing accurate multi-axis forces. Here, we demonstrate a low-cost solution to this problem that integrates four sets of strain gauges, analog-to-digital conversion, and data processing into a single leg of a crab-scale robot. The sensor has a tested range of ± 50 N for contact force and ± 2.5 Nm for torque, which is more than double the weight of a robot made with six such legs. Then, we demonstrate that our sensor is accurate compared to standard, bulkier force gauges and precise enough to be used to differentiate terrains and even find objects buried in sand. Importantly, the sensor has the greatest force load density of any available sensor and more than twice the torque load density of the next best option. This approach to integrating sensors into the most distal appendages can be applied to many other inexpensive end effectors including robot hands, toes, feet, and other tools.

Index Terms—Force sensing, legged robots, object detection.

I. INTRODUCTION

LEGGED robots with smaller form factors are being deployed in new applications, in which accurate contact sensing is critical to control and perception. For example, small crab-like robots are being designed to find unexploded ordnance (UXO) which are hazardous for human handlers [1], [2], [3], [4], [5]. In these applications, vision is not dependable if the object is buried, for example, in soil, sand, or rocks, making control and perception more dependent on contact sensing feedback. Previously proposed contact sensing solutions such as hall-effect sensors [3], [4] or servo current sensors [5] are highly nonlinear. Accurately calibrating for nonlinearity at each leg may require

Received 27 June 2025; accepted 22 October 2025. Date of publication 14 November 2025; date of current version 21 November 2025. This article was recommended for publication by Associate Editor D.-Y. Lee and Editor S.-J. Chung upon evaluation of the reviewers' comments. This work was supported in part by the Office of Naval Research (ONR) under Award N00014-23-1-2842, in part by the Office of Naval Research Young Investigator Program under Award N00014-19-1-2138, and in part by Strategic Environmental Research and Development Program (SERDP) under Award MR19-1369. (Corresponding author: Kathryn A. Daltorio.)

Jianfeng Zhou, Mingyu Pan, and Kathryn A. Daltorio are with the Department of Mechanical and Aerospace Engineering, Case Western Reserve University, Cleveland, OH 44106 USA (e-mail: jxz1113@case.edu; mpx745@case.edu; Kathryn.daltorio@case.edu).

Jiaji Su, Kaiwen Zuo, and Zonghe Chua are with the Department of Electrical, Computer and Systems Engineering, Case Western Reserve University, Cleveland, OH 44106 USA (e-mail: jxs1778@case.edu; kxz365@case.edu; zxc703@case.edu).

This article has supplementary downloadable material available at <https://doi.org/10.1109/LRA.2025.3632679>, provided by the authors.

Digital Object Identifier 10.1109/LRA.2025.3632679

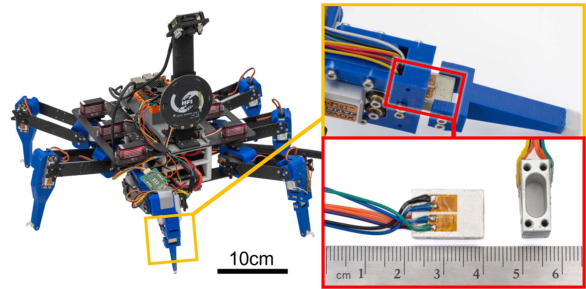


Fig. 1. The sensor is installed on the dactyl of a small crab-like robot.

detailed dynamic actuation models, estimation of magnetic environments, consideration of shielding wear, and larger datasets, which might not make sense at this price point. While uncalibrated contact sensing has been sufficient for some classification problems [3], [4], accurate contact sensing has been shown to enable legged robots to do more, including traversal of more difficult unstructured terrain [6], [7], [8], [9], evaluation of gait efficiency [10], object detection and manipulation [11], [12], and even providing haptic feedback for human-robot interaction [13]. In this work, our goal is to provide the type of accurate contact sensing required for these tasks which are often done with dog-size robots (weight 150 + N), but in a form factor sufficient for a much smaller legged robot (weight 22 N), as shown in Fig. 1.

To sense contact force with legs, unlike robot arms for manufacturing or surgery, the end effector sensors need to support weight and impacts due to locomotion, increasing the requirements for strength and load range. Thus, compliant materials typically used in capacitive force sensors [14], hall effect sensors [15] and pressure-sensitive sheets [16] may not have the required strength and toughness. Because of risk of shattering at impact, a suitable design should avoid utilizing brittle material, such as Piezo elements [17] in micro force sensors [18], or silicon strain gauges (semiconductor strain gauge) [19], [20], [21]. Sensors with foil strain gauges on metal structures [22], [23], [24], [25], [26] have relatively higher stiffness than other sensors, which satisfy the requirements of strength and load range. In addition, to use the same legs for object probing and manipulation [11], [12], [27], [28], multi-axis force sensors [29], [30], [31] can detect contact force in all three dimensions, providing better choices for force vector sensing compared to single-axis force sensors, such as load cells [6] and piezoelectric sensors [7].

To evaluate the load capacity of sensors with different form factors and sizes, a key metric that we propose is the load density. For contact forces, the force load density (FLD) is defined as the fraction of the maximum force load versus the cross-sectional

TABLE I
LOAD DENSITY COMPARISON OF DIFFERENT FORCE SENSORS

Sensor	Size (mm)	FLD (MPa)	TLD (MPa)
P. B.'s [22]	$\varnothing 24.2 \times 42.5$	0.163	0.051
Q. P.'s [16]	$\varnothing 8 \times 15.6$	0.099	0.013
Z. C.'s [18]	$9.5 \times 8.5 \times 23.8$	0.062	0.025
S. M.'s [25]	$\varnothing 9 \times 15$	0.063	0.069
K. L.'s [26]	$\varnothing 10 \times 20$	0.382	0.191
K. U.'s [33]	$\varnothing 14 \times 6.5$	0.195	0.230
K3R70 [36]	$\varnothing 70 \times 12$	0.013	0.011
MiniOne [37]	$\varnothing 30 \times 23.2$	0.071	0.061
MMS101 [38]	$\varnothing 9.6 \times 9$	0.553	0.614
DacSeMo (Ours)	$7 \times 12 \times 18$	0.595	1.653

area, which is equal to the maximum z-axis pressure applied on the sensor. Because torques and moment are also important, the torque load density (TLD) is defined as the fraction of the maximum torque load versus the volume. These ratios are chosen so that both FLD and TLD have comparable units of stress.

These load densities affect not only the leg size, but also the placement of the sensor and thus the design of the end effector. According to previous surveys [29], [30], [31], many existing sensors have relatively lower torque load density, as shown in Table I. Therefore, many sensors are installed directly on the foot tips to reduce the length of the lever arm between contact point and strain gauges [8], [10], [22], [32], which leads to larger foot sizes and more foot structure requirements for adaption, sealing, and protection. In contrast, a larger torque load density allows the sensor to be installed proximal to the joint, allowing larger or interchangeable end effectors to be installed on the sensor [33], which increases the modularity of the robot. In addition, if the robot foot is being used to probe wet, dirty, rough, cohesive, or hazardous environments, (e.g. as in amphibious or surf zones [1], [2], [3], [4], [34], [35]), putting the sensor closer to the joint may reduce the risk of sensor damage by avoiding direct contact with sand or stone.

In this letter, a high load density miniature force sensor is developed for legged robots, specifically addressing the need for probing with feet in field working scenarios. First, the mechanical structure of the new leg-embedded dactyl-sensing module (DacSeMo) is described. Second, the load-to-strain relationships are analyzed, demonstrating the performance under relevant conditions. Based on the load-to-strain model, a calibration matrix is proposed for decoupling. Parameters are then determined through a calibration experiment. This research also presents the development of compact and modular electronic accessories for on-board data processing, especially for mobile robots with limited processing power and no external power source. To the best of our knowledge, as shown in Table I, the sensor design provides greater load density, especially torque load density, compared to commercial sensors [36], [37], [38] and other existing studies with similar force range [22], or with similar size [16], [18], [25], [26], [33]. To validate the performance of the sensor, an error analysis is conducted after calibration to validate the accuracy of the proposed sensor. The sensor is then mounted on a hexapod robot for object detection in sand, allowing us to differentiate contact forces between metal, silicon, and sand. A subsequent test, involving 100,000 sampling times over more than 38 minutes of continuous operation, which is

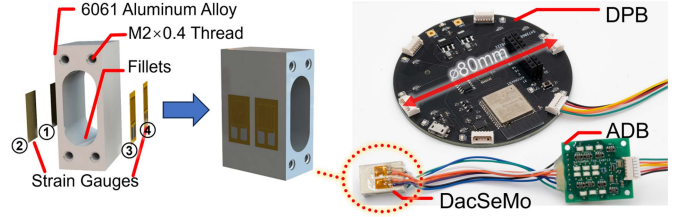


Fig. 2. The three-dimensional force sensor module consists of three main parts: dactyl sensing module (DacSeMo), analog-to-digital converting board (ADB), and data processing board (DPB). The DacSeMo is made of 6061 aluminum alloy with four strain gauges installed on it, customized from PCBWay with tolerance of 0.05 mm and surface roughness of $250 \mu\text{in}/6.3 \mu\text{m}$ Ra. The ADB and DPB are both designed and manufactured by the author with customized PCB from JLCPCB.

longer than expected battery life in outdoor working scenarios, showcases the sensor's robustness.

II. DESIGN AND METHODS

There are three main modules in the force sensor module: dactyl sensing module (DacSeMo), analog-to-digital converting board (ADB), and data processing board (DPB), as shown in Fig. 2. The DacSeMo is the sensing unit installed on the end effector, which transforms the mechanical load into electrical signals via strain sensors. The ADB is a PCB board with amplifiers and analog-to-digital converter to read the voltage of the strain gauges on DacSeMo. To reduce analog noise, the ADB is installed on the robot leg where the DacSeMo is mounted. The DPB is an MCU board for data reading and calibration, installed on the robot body.

A. Mechanical Structure Design of DacSeMo

DacSeMo measures the forces transmitted through the distal linkage of the leg (the dactyl) by replacing a proximal section of the dactyl with the aluminum block on which strain gauges will be mounted. A hollow slot is cut from the aluminum to increase sensitivity, with fillets to prevent stress concentration, as shown in Fig. 2.

There are four strain gauges mounted on the outer wall surface of the slot, with two placed on each side symmetrically. Different from load cells, on which two strain gauges are aligned in a column on each surface near fillets or holes [39], two strain gauges are installed as a parallel pair at the center of DacSeMo corresponding to the straight part of the slot. All strain gauges are installed parallel to the z-axis in the same direction. The structure of DacSeMo is made of 6061-T6 aluminum alloy fabricated with CNC, with a size of $7 \times 12 \times 18$ mm. There are four through holes with screw threads on the DacSeMo for installation on the robot end effector. As shown in Fig. 1, DacSeMo is installed on a hexapod robot dactyl with all strain gauge soldering pads pointing to the proximal side of the foot (aka the positive z-axis points down during walking). The sensor is expected to have the most sensitivity in x-axis direction, corresponding to the movement direction of robot leg, thus we installed DacSeMo with the slot pointing to y-axis direction. The wall thickness of the slot is 1 mm on each side. According to the yield strength of the 6061-T6 aluminum alloy (276 MPa), DacSeMo can withstand a maximum force of ± 177 N in the x-axis and ± 206 N in the y-axis, with the lever arm on the robot dactyl being 5 cm,

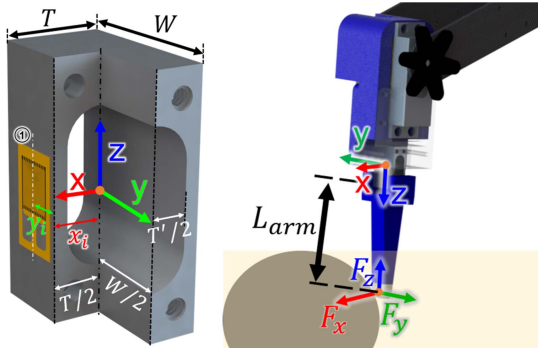


Fig. 3. In the coordinate frame of DacSeMo, W is the width of DacSeMo, T is the thickness of DacSeMo, T' is the width of the hollow slot. In the coordinate frame for contact force on the robot end effector, y -axis and z -axis are in opposite direction to the DacSeMo coordinate frame. During contact with the environment, the three-dimensional forces are transmitted to the DacSeMo via the dactyl as forces and moments.

while in the z -axis, DacSeMo can withstand a maximum force of ± 2800 N. Thus, the strength of the structure fully covers the expected sensor range: ± 100 N in all axis, which is estimated based on the robots' weight range in our lab.

B. Modeling and Simulation

From the four z -axis strains in Fig. 3, Euler-Bernoulli equations can be used to infer moments and forces at the tip. When an x -axis force F_x is applied to the end effector, as shown in Fig. 3, it creates a torque in the y -axis M_y due to the distance (L_{arm}) between the contact point and the sensor. Based on beam theory, the strain can be calculated by

$$\varepsilon_{ix} = -\frac{M_y x_i}{EI_y} = -\frac{12x_i L_{arm}}{EW(T^3 - T'^3)} F_x \quad (1)$$

Ideally for DacSeMo, x_i is half the thickness T , or $x_1 = x_2 = -x_3 = -x_4 = \frac{T}{2}$, although if there are imprecisions in fabrication these values can be adjusted. E is the Young's modulus of the 6061 aluminum alloy. W is the width of DacSeMo. T' is the width of the hollow slot. L_{arm} is the length of the lever arm, shown in Fig. 3, considered equal to the z -axis distance from the effector tip to the threaded holes on DacSeMo.

When the y -axis force F_y is applied to the end effector, it creates a torque in the x -axis, M_x , applied to the DacSeMo. The strain can be calculated by

$$\varepsilon_{iy} = \frac{M_x y_i}{EI_x} = \frac{12y_i L_{arm}}{EW^3(T - T')} F_y \quad (2)$$

Where, if the strain gauges are all installed without misalignment, $y_1 = -y_2 = -y_3 = y_4$.

When a z -axis force F_z is applied to the end effector, the strain can be calculated by

$$\varepsilon_{iz} = \frac{1}{EW(T - T')} F_z \quad (3)$$

From (1), (2), (3), the constant T and T' of the straight slot lead to a uniform strain distribution along z -axis in the strain gauge grid area.

Thus, the overall strain of each strain gauge is

$$\varepsilon_i = \varepsilon_{ix} + \varepsilon_{iy} + \varepsilon_{iz} \quad (4)$$

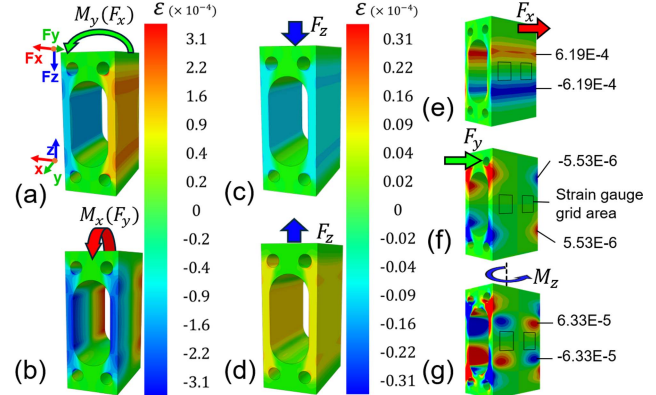


Fig. 4. Strain distribution is analyzed in Abaqus FEA simulation. (a) strain distribution for $+1$ Nm y -axis torque (M_y resulted by x -axis force load F_x) applied to DacSeMo, (b) strain distribution for -1 Nm x -axis torque (M_x resulted by y -axis force load F_y) applied to DacSeMo, (c) strain distribution for $+1$ N z -axis force applied to DacSeMo, (d) strain distribution for -1 N z -axis force applied to DacSeMo, (e) strain distribution for x -axis pure shear force F_x , (f) strain distribution for y -axis pure shear force F_y , (g) strain distribution for z -axis torque M_z .

To better understand the strain distribution on DacSeMo and optimize the placement of the strain gauges, we conducted finite element analysis (FEA) using the static module of Abaqus. As shown in Fig. 4(a), for x -axis force load, the strain is uniformly distributed on the outer surfaces corresponding to the straight part of the slot, except the areas near the edges of DacSeMo. The y -axis load result in Fig. 4(b) shows that the strain on the surface shows a gradient distribution along the y -axis. In the simulation of the z -axis load in Fig. 4(c) and (d), both results show uniformly distributed strain on the outer surface. Thus, for the placement and alignment of the strain gauge in installation, the grid area should be installed on the outer surfaces that correspond to the straight part of the slot, avoiding areas near the edges of DacSeMo and the fillets of the slot.

The effects of the other three dimensional loads can be neglected: pure shear forces (F_x and F_y) and M_z . A pure shear force would only be generated by translational forces applied not at the tip of the dactyl but at the proximal base, for example if a dactyl broke through a thin sheet of ice while being dragged tangentially by an external force. However, most manipulation contact will be near the tip. Simulations of pure shear force in Fig. 4(e) and (f) show negligible strain in the strain gauge grid area, marked as black boxes. Furthermore, because of symmetry, positive and negative strains will tend to cancel. Similarly M_z , equivalent to twisting motions about the dactyl will be both unlikely due to the way the leg is actuated, and have small effects shown in Fig. 4(g).

The strain values at four different positions ($x_i = \pm 3.5$ mm, $y_i = \pm 2.5$ mm, $z_i = 0$ mm) on DacSeMo are measured under different loads. These positions correspond to the center of the strain gauge grids. The results are shown in Fig. 6(a), demonstrating the linear relationship between strain and load.

C. Design of Electronics Accessories

To detect the voltage changes of the strain gauges, a four-channel ADC with customized gain is required. To satisfy the requirements of being lightweight and compact for on-board

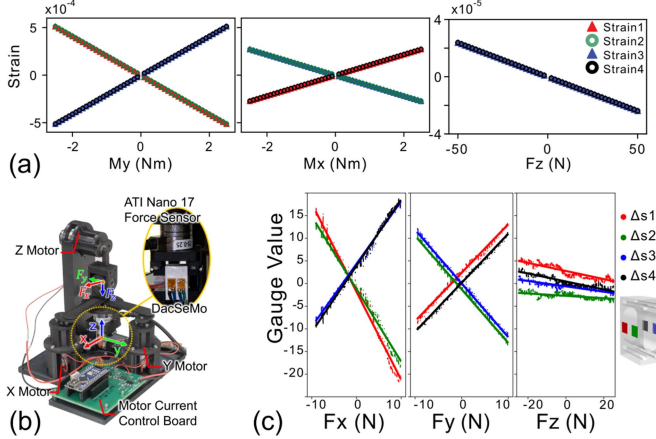


Fig. 6. (a) Abaqus FEA simulation results of strain (ε_i) versus load. (b) The linkage and three-DoF hinge on the calibration platform make it able to apply load in three dimensions independently. (c) Strain gauge values (Δs_i) versus the reference force in each of the three dimensions. Solid lines represent best linear fits to the calibration data.

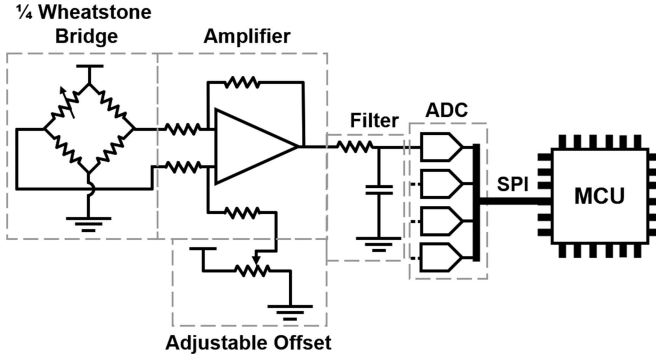


Fig. 5. There are four analog channels on each ADB. Each channel consists of a quarter Wheatstone bridge, an amplifier (MCP6H04, Gain=10000) with adjustable offset, a low-pass filter with a cutoff frequency of 338 Hz, and a channel of ADC (AD7811). The ADB uses SPI to communicate with the DPB.

processing on a small mobile robot, we designed and built the ADB that can be carried and powered by the robot itself. We then designed and built the DPB to convert the strain gauge voltage to three-dimensional force.

There are four channels on each ADB, each channel detecting the voltage of one strain gauge using a quarter Wheatstone bridge, as shown in Fig. 5. The output of the bridge is connected to a differential amplifier (MCP6H04, Microchip Technology, Chandler, AZ) to amplify the voltage difference. Theoretically, when there is no load on the strain gauge, the strain gauge voltage offset and the amplifier output voltage offset should be both 2.5 V, in a range of 0-5 V. However, preload force during the strain gauge installation procedure can induce strain gauge offset error in most cases. The offset error can also be caused by the resistance error and the manufacturing error on the DacSeMo surface. The offset error may cause the output voltage to saturate after passing through the amplifier. Thus, an adjustable offset is added to the differential amplifier to keep the output voltage in range. The amplified signal is then input into one channel of the ADC (AD7811, Analog Devices, Wilmington, MA) after

passing the low-pass filter, and after conversion, it is transmitted to the MCU on the DPB via SPI.

The DPB is designed to receive the SPI signal from the ADB and upload the calibrated force data through the micro-USB port. It mainly consists of an MCU (ESP32-WROOM-32E, Espressif Systems, Shanghai, Shanghai), a USB-to-UART bridge (CP2104, Silicon Labs, Austin, TX), and a multiplexer (SN74HCS251, Texas Instruments, Dallas, TX). There are six ports that enable the DPB to connect six sensors. The multiplexer makes the MCU capable of selecting one sensor's input signal from all six ports. The USB-to-UART bridge enables the MCU to communicate with the supervisory computer (or the single-board computer on the robot) with a maximum baud rate of 2 Mbit/s.

Before force detection, the DPB first measures all channels on the selected sensor to initialize the offset without any load, for example, when the robot leg is in a swing-phase in the air. The initialization also helps to eliminate the influence of nonuniform screw-tightening torque during installation. Following initialization, the strain gauge data are fed into a Kalman filter and a moving average smoothing filter, and subsequently transformed into three-dimensional force data. The force data are then converted into serial buffer as a bytes array for serial communication. By adding a flipping logic output on a digital pin, we can measure the sampling period on an oscilloscope, which is 1.4 ms at a baud rate of 2 Mbit/s and 4 ms at a baud rate of 115200 bits/s. Thus, the on-board sampling rate can reach up to 700 Hz.

III. CALIBRATION

A calibration step is needed to convert the voltage of the strain gauges into three-dimensional force.

A. Decoupling and Calibration for the Sensors

Due to the linearity of the strain gauges and amplifiers, the change in the reading value of the voltage of each strain gauge Δs_i is proportional to the strain.

$$\Delta s_i = s_i - s_{i0} = k\varepsilon_i = k_{ix}F_x + k_{iy}F_y + k_{iz}F_z \quad (5)$$

s_{i0} is the offset of each strain gauge and s_i is the value of each strain gauge. Thus, the relationship between sensor values and force is as follows.

$$\Delta s = \begin{bmatrix} \Delta s_1 \\ \Delta s_2 \\ \Delta s_3 \\ \Delta s_4 \end{bmatrix} = \begin{bmatrix} k_{1x} & k_{1y} & k_{1z} \\ k_{2x} & k_{2y} & k_{2z} \\ k_{3x} & k_{3y} & k_{3z} \\ k_{4x} & k_{4y} & k_{4z} \end{bmatrix} \begin{bmatrix} F_x \\ F_y \\ F_z \end{bmatrix} = \mathbf{K}\vec{F} \quad (6)$$

A state vector \vec{S} is defined as

$$\vec{S} = \begin{bmatrix} s_x \\ s_y \\ s_z \end{bmatrix} = \begin{bmatrix} 1 & 1 & -1 & -1 \\ 1 & -1 & -1 & 1 \\ 1 & 1 & 1 & 1 \end{bmatrix} \Delta s = \mathbf{M}\Delta s \quad (7)$$

in which \mathbf{M} is a mapping matrix that maps the 4×1 strain gauge values Δs into the 3×1 state vector \vec{S} .

Thus, taking (6) into (7), the relationship of the state vector \vec{S} and the force vector \vec{F} is

$$\vec{S} = \mathbf{M}\mathbf{K}\vec{F} = \mathbf{K}_m\vec{F} \quad (8)$$

in which \mathbf{K}_m makes a 3×3 invertible matrix. Thus, the force vector \vec{F} can be calculated by

$$\vec{F} = \mathbf{K}_m^{-1} \vec{S} = \mathbf{C} \vec{S} \quad (9)$$

\mathbf{C} is the calibration matrix that is used in the calibration step for on-board processing in the DPB.

From (1), (2), (3) and the FEA simulation results (shown in Fig. 6(a)), we could expect equal proportionality coefficients k_{ix} , k_{iy} , k_{iz} for each strain gauge, making the theoretical calibration matrix a diagonal matrix. However, fabrication tolerance and surface roughness in CNC, sensor misalignment in manual installation, and differential amplifier circuits induce random factors in the system, leading to unequal proportionality coefficients for each strain gauge in (5). Thus, a calibration test is designed to measure and estimate the proportionality coefficients for each strain gauge.

B. Calibration Experiment

For the calibration experiment, we designed and built a calibration platform, as shown in Fig. 6(b). The DacSeMo is fixed on the base with an ATI Nano 17 F/T sensor fixed on the DacSeMo tip. A load pad is mounted on the ATI Nano 17 F/T sensor. There are three geared DC motors to load force in each axis, all controlled by the motor current control board. The X motor and the Y motor are connected to the load pad via a bar linkage with bearings to ensure that no extra torque is applied to the linkage and sensors. The Z motor is connected to the load pad through a 2-degree-of-freedom hinge to avoid sharing forces in the x and y directions. Therefore, the load in each direction is independent.

During the experiment, the motor current control board and the ATI Nano 17 F/T sensor are connected to a supervisory computer for load control and standard force detection. The DacSeMo is also connected to the same computer via the ADB and the DPB to record the measured values for all strain gauges (Δs_i). After setting up the communication on the computer, the current control board started to load in one direction. For the load in the x and y direction, the load force started from -10 N to +10 N while the z load started from -20 N to +20 N. The force step size is 0.4 N for all directions. For each force value, the computer recorded 100 groups of values from the ATI Nano 17 F/T sensor and the strain gauges, as shown in Fig. 6(c). The slopes of the fitted lines are the proportionality coefficients k_{ix} , k_{iy} , k_{iz} for the corresponding strain gauge, representing the sensitivity of each strain gauge to load in each dimension, shown in (10).

$$\mathbf{K} = \begin{bmatrix} -1.9474 & 1.0699 & -0.0893 \\ -1.6050 & -1.1813 & -0.0261 \\ 1.3863 & -1.1845 & -0.0593 \\ 1.4649 & 1.0816 & -0.088 \end{bmatrix} \quad (10)$$

Thus, we can calculate the calibration matrix from (8), (9), (10)

$$\mathbf{C} = \begin{bmatrix} -0.1541 & -0.0012 & -0.0183 \\ -0.0006 & 0.2178 & -0.0763 \\ 0.4119 & -0.1745 & -3.6956 \end{bmatrix} \quad (11)$$

in which the absolute values of the diagonal elements represent the force corresponding to unit value of the strain gauges (ADC voltage resolution). Therefore, the sensitivity of the sensor in each dimension can be calculated as the fraction of voltage

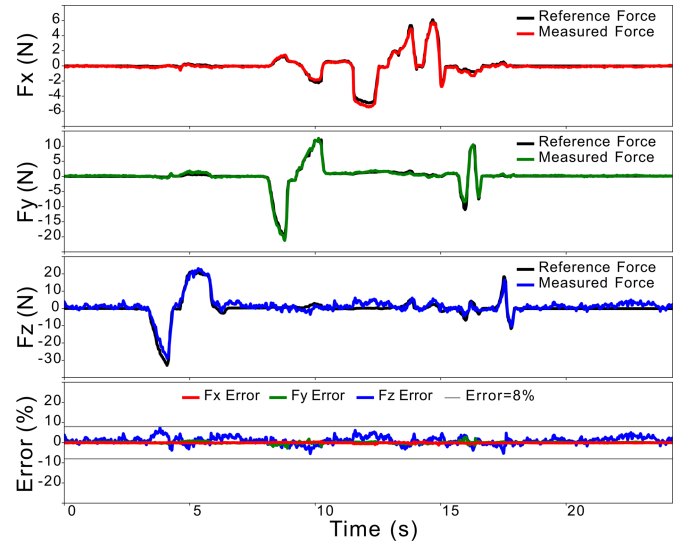


Fig. 7. Measured force from the force sensor versus the reference force in each of the three dimensions. The maximum Max-Instant Error is in z-axis, which is mainly caused by the dynamic effect of the moving average smoothing filter.

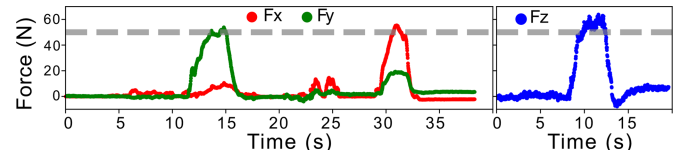


Fig. 8. Force range is demonstrated with a Nextech DFS50 Force Gauge. The maximum force load in each dimension is above 50 N. The length of lever arm for loads in x-axis and y-axis is 5 cm, making the maximum torque loads above 2.5 Nm.

resolution over unit force: 31.69 mV/N in x-axis, 22.42 mV/N in y-axis, and 1.32 mV/N in z-axis.

IV. RESULTS

A. Accuracy Analysis

In order to demonstrate the performance of the sensor module proposed in this letter, a second experiment is done on the calibration platform. In this experiment, the DPB is coded with the calibration matrix and uploaded the three-dimensional force data directly to the supervisory computer. To simulate working conditions, a user touched the load pad directly with random dynamic forces while the supervisory computer recorded the real-time force values of the ATI Nano 17 F/T sensor and the proposed sensor module. As shown in Fig. 7, the force value of the ATI Nano 17 F/T sensor is colored red as the reference force while the force value of the proposed sensor module is colored blue as the measured force.

To avoid damaging the ATI Nano 17 F/T sensor, the theoretical range of ± 100 N ($\hat{F}_{range} = 200$ N) is not reached in this experiment, instead a tested range force of ± 50 N ($F_{range} = 100$ N) is used for all dimensions to normalize errors, as shown in Fig. 8. The real-time errors of three directions are also shown in Fig. 7, from which the maximum instantaneous errors of all dimensions are within the range of $\pm 8\%$. The average error and the Normalized Root Mean Square Error (NRMSE) are shown

TABLE II
ERRORS IN EACH OF THE THREE DIMENSIONS

	NRMSE(%)	Max-Instant Error(%)
F_x	0.17	0.66
F_y	0.39	2.71
F_z	2.13	7.63

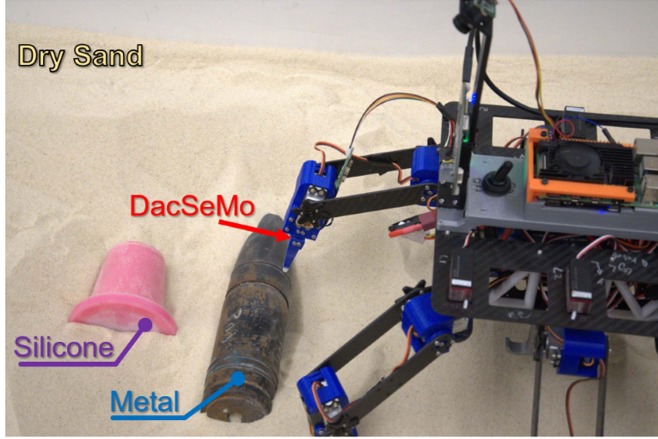


Fig. 9. On-Robot test is set up in sandbox. The foot tip moves in a straight trajectory in the x-axis direction at a constant speed.

in Table II. The sensor has the best performance on the x-axis with the lowest NRMSE of 0.17% and the lowest Max-Instant Error of 0.66%. The NRMSE on all three dimensions are below 3%.

B. Legged Robot Searching for Objects in Sand

To demonstrate the application of the proposed force sensor module in a robot end effector, a series of on-robot tests are conducted. We installed DacSeMo on a foot tip of a hexapod robot in our lab and placed the robot in a sandbox, as shown in Fig. 9. The weight of the robot is 22 N, and the servo's stall torque is 2 Nm, making the contact force in the range of the sensor. The goal of our robot is to detect artificial debris on the beach, such as unexploded ordnance (UXO), etc. Therefore, a metal UXO model is used to simulate hard material targets. The robot stood resting on the other five legs, while the sensorized leg is lifted and moved back and forth in the x-axis direction to touch objects to simulate object detection in field settings. In order to test whether the proposed sensor can distinguish material stiffness based on the real-time force signal, a silicone object is used to simulate organisms for comparison.

The first experiment is conducted with both objects out of the sand, while the robot touched the object at a constant speed of 1.5 cm/s in the x-axis and measured the three-dimensional force in real time. The results of the metal object and silicone object are shown in Fig. 10. During the experiments, the first peak always has a steep rising edge due to initialization, during which the robot leg moves quickly to its initial position and kicks the object. Thus, the first peak is removed when we plotted and analyzed the waveforms over a single movement period, as shown in the right column of Fig. 10. As shown in the period plot, it can be seen that the force waveform for every contact is almost identical. Because of the direction of foot tip movement during the experiment, the contact force in the x direction exhibited the

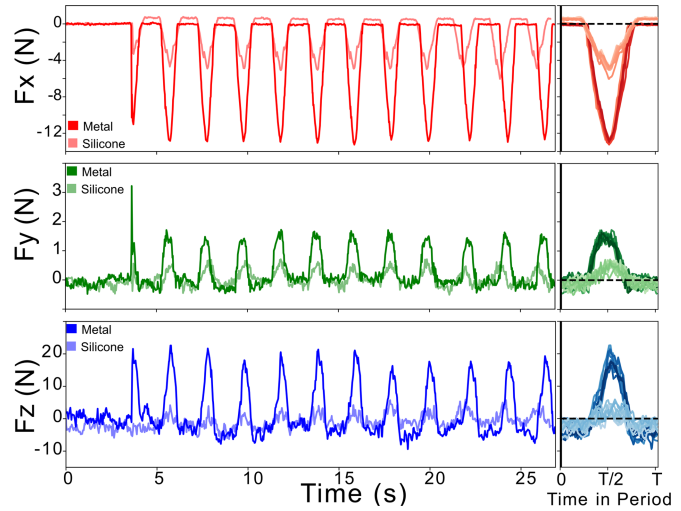


Fig. 10. Three dimensional contact force is measured for contacting object at a constant speed of 1.5 cm/s and a constant frequency of 0.5 Hz. Force waveforms from the 2nd peak to the 11th peak are plotted in period on the right.

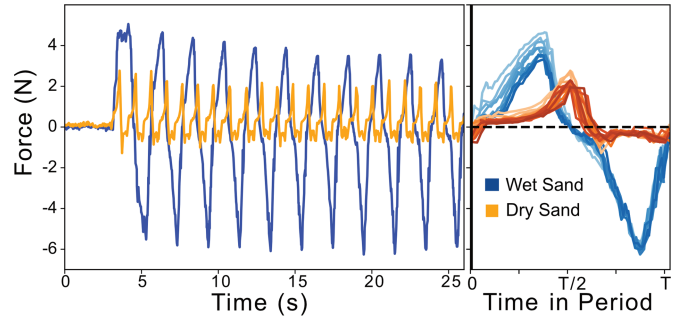


Fig. 11. X-axis force is measured for contact with sand. For the dry sand test, force waveforms from the 2nd peak to the 21st peak are plotted in period on the right. For the wet sand test, force waveforms from the 2nd peak to the 11th peak are plotted in period on the right.

most significant change and the smoothest waveform, making the x-axis force the primary basis for our analysis. Comparing the two results, it can be seen that the changing rate of x-axis force is larger when contacting metal, which indicates a higher stiffness of the material.

Next, we compare force signatures when probing wet and dry sand. In dry sand, if the robot moves too slowly, the granular media resistance is too small to detect. In wet sand, the ground reaction forces are larger. To prove that different forces are evident even if the speed control is imprecise, we move the leg faster in dry sand (at a constant speed of 3 cm/s in x-axis and a frequency of 1 Hz) and slower in wet sand (at a constant speed of 1.5 cm/s at a frequency of 0.5 Hz). The results of the contact force in the x-axis are shown in Fig. 11, which display distinct waveforms and magnitudes in each environment. Specifically, we can see that the wet sand peak is twice the dry sand peak, even when we give the wet sand the handicap of moving at half speed. This suggests that our robot will be able to reliably detect when walking on wet vs. dry sand, which will enable it to walk efficiently.

Then another experiment is conducted to detect objects buried in dry sand, as shown in Fig. 12(a). During the test, the metal

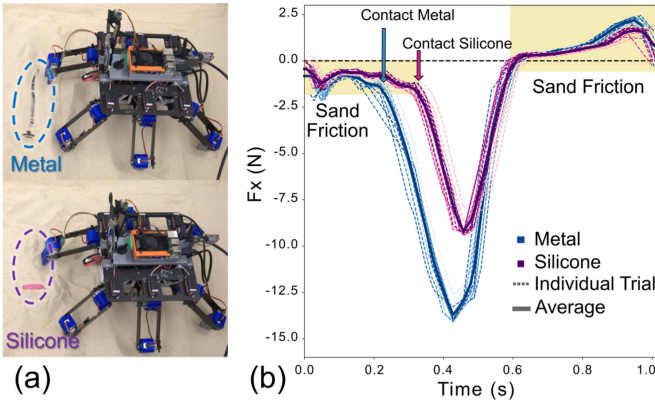


Fig. 12. (a) Objects are buried in dry sand for probing test. (b) Periodic x-axis contact force profiles where the robot repeatedly probes the metal object and silicone object in sand.

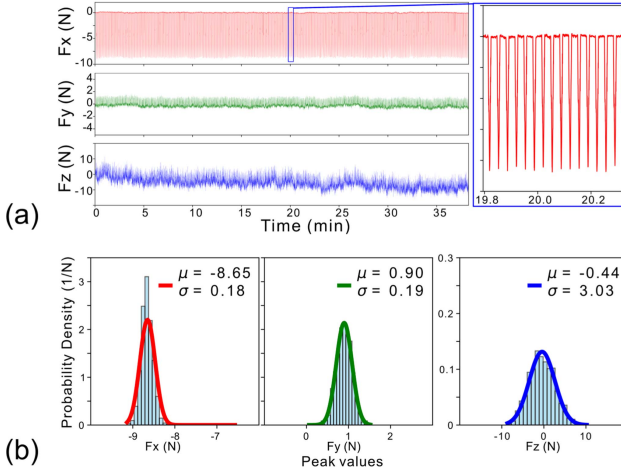


Fig. 13. (a) Entire duration of the periodic three-dimensional force for robustness test and force peaks in x-axis (b) Normal distribution of peak values of the three-dimensional force.

object and the silicone object are covered with dry sand, while the robot moved the foot tip in the sand to touch the object at a constant speed of 1.5 cm/s at a frequency of 1 Hz. The results of the contact force over a single period are shown in Fig. 12(b), highlighting the difference in contact force between sand, metal, and silicone objects.

C. Robustness Test

A repeat test is conducted to demonstrate the robustness of the proposed sensor module. During the test, the robot repeatedly contacts the metal object at a frequency of 0.5 Hz, while the supervisory computer records 100,000 samples in MATLAB at approximately 40 Hz, with the sensor being initialized only at the beginning. The entire test took approximately 38 minutes, which exceeds the expected battery life in outdoor deployment scenarios. The results of the three-dimensional contact force are shown in Fig. 13(a), which shows stable force data in the x-axis and y-axis after a long-duration test. An overall drift is observed in the z-axis force, which is a temperature drift caused by long-duration work. The peaks of F_x from 19.8 min to 20.2 min are

TABLE III
SPECIFICATIONS OF THE PROPOSED FORCE SENSOR MODULE

Specifications	Description
DacSeMo Size	$7 \times 12 \times 18$ mm
PCB Size	ADB: 28×25 mm, DPB: $\phi 80$ mm
Range	Tested: ± 50 N / ± 2.5 Nm Theoretical: ± 100 N / ± 5.0 Nm
Power Supply	5 V USB / 2S LiPo Battery
Interface	USB / UART
MAX Sample Rate	700 Hz
Total Cost	$\leq \$30$

shown in Fig. 13(a). The time stamps of the F_x peaks are used to define the peaks for F_y and F_z .

The normal distributions of the peak values of each dimension are shown in Fig. 13(b) to better evaluate the robustness. The standard deviation of F_x ($\sigma = 0.18$) and F_y ($\sigma = 0.19$) demonstrate that the sensor shows strong robustness and stability in x-axis and y-axis. The standard deviation of F_z ($\sigma = 3.03$) also indicates that the sensor can maintain a relatively stable output in the z-axis even with the temperature of the ADB increasing over time during the experiment.

V. CONCLUSION AND DISCUSSION

In this letter, we show that accurate, compact, and high-range foot force sensing is possible for a small, low-cost, walking robot, which enables the robot to probe with its foot and detect object buried in sand. The final specifications of the sensor module are shown in Table III.

Compared with the commercial sensors and other existing studies with similar range [22], [36], [37], [38], or with similar size [16], [18], [25], [26], [33], we can conclude that the main advantages of this design are the following: (1) Simple design of the structure, simplifying fabrication and reducing the cost while ensuring strength and robustness; (2) Miniature size and low weight with high load density, suitable for sensorizing a compact end effector on a robot that may face high load working conditions; (3) On-board processing, eliminating the need for additional power sources and signal analyzer, reducing weight and making it particularly advantageous for mobile robots such as legged robots; (4) Achieving high accuracy in the x-axis and y-axis comparable to commercial sensors at a significantly lower cost. With these advantages, we propose that this sensor module can provide an easy and inexpensive solution for three-dimensional force sensing on end effectors, such as finger tips on robot hand, which can contribute to the development of robot manipulation and enable haptic feedback. Furthermore, this study can lead to exploration of the relationship between load density and mechanical design of the sensor, such as the relationship between sensor width and stiffness in [24].

The design of DacSeMo also makes it flexible in terms of sensor size. From Figs. 3 and 4, it can be inferred that the minimum size of DacSeMo design requires the straight part of the slot to be no less than the length of strain gauge grid, and the width of DacSeMo, W , to be greater than the width of two strain gauges' grid. Therefore, the minimum size of DacSeMo can be reduced by using smaller strain gauges. For example, the size of DacSeMo can be reduced to $6\text{mm} \times 6\text{mm} \times 12\text{mm}$ by using OMEGA SGT-2 series strain gauges, which could potentially be applied on the fingertip of a humanoid robot or insect-like millirobots [40]. Furthermore, the strain distribution of different

loads in Fig. 4 indicates the possibility of developing a 6-DoF force/torque sensor by attaching more strain gauges to a larger DacSeMo.

However, z-axis measurements are less reliable compared to commercial sensors, due to the low sensitivity of the structure to z-axis loads and the relatively low resolution of the ADC. Performance can be enhanced by using an ADC with higher resolution, such as a 16-bit ADC, for more accurate voltage sampling. Higher resolution can also reduce the reliance on smoothing filters, which helps decrease the Max-Instant Error caused by the dynamic effect of filters. Reducing the wall thickness or width of the DacSeMo can also improve sensitivity, but would also potentially reduce strength. Additional initialization and calibration of offset and/or adding an extra temperature compensation resistor to the ADB can provide real-time adjustments to account for temperature fluctuations, reducing the drift of the z-axis measurement over the robustness test.

REFERENCES

- [1] N. M. Graf, A. M. Behr, and K. A. Daltorio, "Dactyls and inward gripping stance for amphibious crab-like robots on sand," *Bioinspiration Biomimetics*, vol. 16, no. 2, Mar. 2021, Art. no. 026021.
- [2] N. M. Graf, J. E. Grezmak, and K. A. Daltorio, "Get a grip: Inward dactyl motions improve efficiency of sideways-walking gait for an amphibious crab-like robot," *Bioinspiration Biomimetics*, vol. 17, no. 6, Nov. 2022, Art. no. 066008.
- [3] J. Grezmak, N. Graf, A. Behr, and K. Daltorio, "Terrain classification based on sensed leg compliance for amphibious crab robot," *IEEE Sensors J.*, vol. 21, no. 20, pp. 23308–23316, Oct. 2021.
- [4] J. Grezmak and K. A. Daltorio, "Probing with each step: How a walking crab-like robot classifies buried cylinders in sand with hall-effect sensors," *Sensors*, vol. 24, no. 5, Feb. 2024, Art. no. 1579.
- [5] Y. Gong, M. Pan, and K. A. Daltorio, "Using a small hexapod robot to pick up large cylinders for munitions response," *J. Field Robot.*, Nov. 2024, Art. no. rob.22482.
- [6] M. Cao, K. Yamashita, T. Kiyozumi, and Y. Tada, "Hexapod robot with ground reaction force sensor on rough terrain," in *Proc. 2021 IEEE Int. Conf. Mechatron. Automat.*, Takamatsu, Japan, Aug. 2021, pp. 1088–1093.
- [7] G. Picardi, M. Chellapurath, S. Iacoponi, S. Stefanni, C. Laschi, and M. Calisti, "Bioinspired underwater legged robot for seabed exploration with low environmental disturbance," *Sci. Robot.*, vol. 5, no. 42, May 2020, Art. no. eaaz1012.
- [8] R. Kaslin, H. Kolvenbach, L. Paez, K. Lika, and M. Hutter, "Towards a passive adaptive planar foot with ground orientation and contact force sensing for legged robots," in *Proc. 2018 IEEE/RSJ Int. Conf. Intell. Robots Syst.*, Madrid, Oct. 2018, pp. 2707–2714.
- [9] H. Zhang et al., "A force-sensing system on legs for biomimetic hexapod robots interacting with unstructured terrain," *Sensors*, vol. 17, no. 7, Art. no. 1514, Jun. 2017.
- [10] H. Gao et al., "Low impact force and energy consumption motion planning for hexapod robot with passive compliant ankles," *J. Intell. Robotic Syst.*, vol. 94, no. 2, pp. 349–370, May 2019.
- [11] X. Ding and F. Yang, "Study on hexapod robot manipulation using legs," *Robotica*, vol. 34, no. 2, pp. 468–481, Feb. 2016.
- [12] K. Inoue, K. Ooe, and S. Lee, "Pushing methods for working six-legged robots capable of locomotion and manipulation in three modes," in *Proc. 2010 IEEE Int. Conf. Robot. Automat.*, Anchorage, AK, USA, May 2010, pp. 4742–4748.
- [13] P. Xu et al., "A closed-loop shared control framework for legged robots," *IEEE/ASME Trans. Mechatron.*, vol. 29, no. 1, pp. 190–201, Feb. 2024.
- [14] U. Kim, Y. B. Kim, D.-Y. Seok, J. So, and H. R. Choi, "A surgical palpation probe with 6-Axis force/torque sensing capability for minimally invasive surgery," *IEEE Trans. Ind. Electron.*, vol. 65, no. 3, pp. 2755–2765, Mar. 2018.
- [15] S. D. Moosavi Nasab, A. Beiranvand, M. Tale Masouleh, F. Bahrami, and A. Kalhor, "Design and development of a multi-axis force sensor based on the hall effect with decouple structure," *Mechatronics*, vol. 84, Jun. 2022, Art. no. 102766.
- [16] Q. Pan, J. Luo, L. Chen, H. Xue, and H. Wang, "A modular miniature 6-D force sensor designed for minimally invasive surgery," *IEEE Trans. Instrum. Meas.*, vol. 73, 2024, Art. no. 9516711.
- [17] Alpsalpine, "ForceSensor HSFPAR003 A data sheet," 2019. [Online]. Available: https://www.mouser.com/datasheet/2/15/product_spec_hsfpars003a_en_5bae2e5d1e-3473838.pdf
- [18] Z. Chua and A. M. Okamura, "A modular 3-Degrees-of-Freedom force sensor for robot-assisted minimally invasive surgery research," *Sensors*, vol. 23, no. 11, May 2023, Art. no. 5230.
- [19] Honeywell, "FMA SERIES MicroForce sensors, compensated/amplified," 2020. [Online]. Available: https://mm.digikey.com/Volume0/opasdata/d220001/medias/docus/448/FMA_Series_DS.pdf
- [20] R. Tamura, T. Horikoshi, S. Sakaino, and T. Tsuji, "High dynamic range 6-axis force sensor employing a semiconductor–metallic foil strain gauge combination," *IEEE Robot. Automat. Lett.*, vol. 6, no. 4, pp. 6243–6249, Oct. 2021.
- [21] Honeywell, "FSS-SMT series low profile force sensor," 2014. [Online]. Available: <https://www.mouser.com/datasheet/2/187/honeywell-sensing-force-sensors-FSS-SMT-product-sh-1128716.pdf>
- [22] P. Billeschou, C. Albertsen, J. C. Larsen, and P. Manoonpong, "A low-cost, compact, sealed, three-axis force/torque sensor for walking robots," *IEEE Sensors J.*, vol. 21, no. 7, pp. 8916–8926, Apr. 2021.
- [23] R. Shu, Z. Chu, H. Jiao, and H. Shu, "Contact force sensing of L-shaped structure for robotic end-effectors," *IEEE/ASME Trans. Mechatron.*, vol. 29, no. 1, pp. 455–465, Feb. 2024.
- [24] T. Kawahara and T. Tsuji, "Development of an easy-to-cut six-axis force sensor," *IEEE Robot. Automat. Lett.*, vol. 9, no. 1, pp. 563–570, Jan. 2024.
- [25] S. Matich, M. Hessinger, M. Kupnik, R. Werthschützky, and C. Hatzfeld, "Miniaturized multiaxial force/torque sensor with a rollable hexapod structure: Miniaturisierter kraft-momenten-sensor AUF basis einer gerollten hexapod-struktur," *tm -Technisches Messen*, vol. 84, no. s1, pp. 138–142, Sep. 2017.
- [26] K. Li, B. Pan, Y. Fu, and S. Wang, "Experimental study of static and dynamic characteristics of a miniature 6-axis force and torque sensor," in *Proc. 2015 IEEE Int. Conf. Inf. Automat.*, Lijiang, China, Aug. 2015, pp. 1579–1584.
- [27] X. Cheng, A. Kumar, and D. Pathak, "Legs as manipulator: Pushing quadruped agility beyond locomotion," in *Proc. 2023 IEEE Int. Conf. Robot. Automat.*, London, U.K., May 2023, pp. 5106–5112.
- [28] Y. Ji, G. B. Margolis, and P. Agrawal, "DribbleBot: Dynamic legged manipulation in the wild," in *Proc. 2023 IEEE Int. Conf. Robot. Automat.*, London, U.K., May 2023, pp. 5155–5162.
- [29] M. Y. Cao, S. Laws, and F. R. Y. Baena, "Six-axis force/torque sensors for robotics applications: A review," *IEEE Sensors J.*, vol. 21, no. 24, pp. 27238–27251, Dec. 2021.
- [30] J. O. Templeman, B. B. Sheil, and T. Sun, "Multi-axis force sensors: A state-of-the-art review," *Sensors Actuators A: Phys.*, vol. 304, Art. no. 111772, Apr. 2020.
- [31] S. Li and J. Xu, "Multi-axis force/torque sensor technologies: Design principles and robotic force control applications: A review," *IEEE Sensors J.*, vol. 35, no. 3, pp. 4055–4069, Feb. 2025.
- [32] Y. Su et al., "A unified foot-terrain interaction model for legged robots contacting with diverse terrains," *IEEE/ASME Trans. Mechatron.*, vol. 29, no. 4, pp. 2661–2672, Aug. 2024.
- [33] U. Kim, H. Jeong, H. Do, J. Park, and C. Park, "Six-axis force/torque fingertip sensor for an anthropomorphic robot hand," *IEEE Robot. Automat. Lett.*, vol. 5, no. 4, pp. 5566–5572, Oct. 2020.
- [34] D. A. Vasquez, D. Jay, M. Dina, M. Austin, S. McConomy, and J. E. Clark, "Design of STARQ: A multimodal quadrupedal robot for running, climbing, and swimming," in *Proc. 2023 IEEE/RSJ Int. Conf. Intell. Robots Syst.*, Detroit, MI, USA, Oct. 2023, pp. 2746–2751.
- [35] R. Baines et al., "Multi-environment robotic transitions through adaptive morphogenesis," *Nature*, vol. 610, no. 7931, pp. 283–289, Oct. 2022.
- [36] ME-Meßsysteme, "K3R70," 2024. [Online]. Available: <https://www.me-messsysteme.de/en/k3r70-50n>
- [37] Botasys, "MiniONE," 2024. [Online]. Available: <https://www.botasys.com/force-torque-sensors/minione>
- [38] Mitsumi, "MMS101 data sheet," 2022. [Online]. Available: https://cdn.nmbtc.com/uploads/2022/03/mms101_datasheet_en_rev4.1.pdf
- [39] D. Trent, "How does a strain gauge work?" 2020. [Online]. Available: <https://www.800loadcel.com/load-cell-and-strain-gauge-basics.html>
- [40] D. W. Haldane et al., "Integrated manufacture of exoskeletons and sensing structures for folded millirobots," *J. Mechanisms Robot.*, vol. 7, no. 2, May 2015, Art. no. 021011.